

# Fast Robust Dejitter and Interslice Discontinuity Removal in MRI Phase Acquisitions: Application to Magnetic Resonance Elastography

Eric Barnhill<sup>1</sup>, *Member, IEEE*, Mila Nikolova, Cemre Ariyurek, Florian Dittmann, Jürgen Braun, *Member, IEEE*, and Ingolf Sack, *Member, IEEE*

**Abstract**—MRI phase contrast imaging methods that assemble slice-wise acquisitions into volumes can contain interslice phase discontinuities (IPDs) over the course of the scan from sources, including unavoidable physiological activity. In magnetic resonance elastography (MRE), this can alter wavelength and tissue stiffness estimates, invalidating the analysis. We first model this behavior as jitter along the z-axis of the phase of 3D complex-valued wave volumes. A two-step image processing pipeline is then proposed that removes IPDs. First, constant slice-wise phase shift is removed with a novel, non-convex dejittering algorithm. Then, regional physiological noise artifacts are removed with novel filtering of 3D wavelet coefficients. Calibration of two pipeline coefficients, the dejitter parameter  $\alpha$  and the wavelet band high-pass coefficient  $\omega_c$ , was first performed on a finite-element method brain phantom. A comparative investigation was then performed, on a cohort of 48 brain acquisitions, of four approaches to IPDs: 1) the proposed method; 2) a “control” condition of neglect of IPDs; 3) an anisotropic wavelet-based method; and 4) a method of in-plane (2D) processing. The present method showed medians of  $|G^*| = 1873$  Pa for a multifrequency wave inversion centered at 40 Hz which was within 6% of methods 3) and 4), while neglect produced  $|G^*|$  estimates a mean of 17% lower. The proposed method reduced the value range of the cohort against methods 3) and 4) by 29% and 31%, respectively. Such reduction in variance enhances the ability of brain MRE to predict subtler physiological changes. Our theoretical approach further enables more

powerful applications of fundamental findings in noise and denoising to MRE.

**Index Terms**—Magnetic resonance imaging, elastography, image denoising.

## I. INTRODUCTION

MRI phase contrast imaging manipulates magnetic field gradients to create images of *in vivo* motion and flow [22]. Several of the many methods that exploit phase contrast require evaluation of 3D image volumes [27], [37]. However, for reasons of signal-to-noise ratio (SNR) it is frequently advantageous to obtain the images slice-wise, exposing the inter-slice integrity of the volume to artifact from patient movement or physiological movement over the course of the scan.

One such phase-contrast modality is magnetic resonance elastography (MRE) [13], which coordinates motion-sensitized encoding gradients with shear wave motion induced by an external driver to obtain phase images of shear wave propagation. Tissue mechanical properties, most commonly the complex shear modulus, can then be assessed via wave inversion. While some approaches to magnetic resonance elastography (MRE) reconstruction use an in-plane reconstruction approach [31], [38], many approaches evaluate the full 3D wave propagation, in which case artifact between slices will, if left untreated, alter wavelength estimates along the  $z$  axis, resulting in severe error in wavelength estimation.

Such wavelength estimation errors are distinct from the more typical, larger-scale, inter-volume patient motion handled by, for example, neuroimaging software (e.g. Smith *et al.* [35]) or abdominal MRI motion correction (e.g. Zuo *et al.* [39]). These motion correction methods were incorporated into MRE image processing as a preliminary step in recent work [8]. MRE, being a phase-based imaging method, is sensitive to much smaller, micron-order motions occurring within a scan of a single volume, and is consequently exposed to artifact at this scale. We refer to this second artifact here as interslice phase discontinuities (IPDs).

The presence of cardiac-related pulsatile motion in the brain, as well as its encoding and measurement with phase-based

Manuscript received October 10, 2018; revised January 2, 2019; accepted January 10, 2019. Date of publication January 25, 2019; date of current version June 28, 2019. This project has received funding from the European Unions Horizon 2020 research and Innovation programme under grant agreement No 668039 and the European Unions Seventh Framework Programme for research, technological development and demonstration under grant agreement No FP7-ICT- 2011-9-601055. (Corresponding author: Eric Barnhill.)

E. Barnhill is with iRhythm Technologies, San Francisco, CA 94103 USA (e-mail: ebarnhill@irhythmtech.com).

M. Nikolova, deceased, was with CMLA, ENS Cachan, CNRS, Université Paris-Saclay, 94235 Cachan, France.

C. Ariyurek is with the National Magnetic Resonance Research Center (UMRAM), Bilkent University, Ankara 06800, Turkey.

F. Dittmann and I. Sack are with the Department of Radiology, Charité—Universitätsmedizin Berlin, 10117 Berlin, Germany.

J. Braun is with the Institute for Medical Informatics, Charité—Universitätsmedizin Berlin, 10117 Berlin, Germany.

Color versions of one or more of the figures in this paper are available online at <http://ieeexplore.ieee.org>.

Digital Object Identifier 10.1109/TMI.2019.2893369

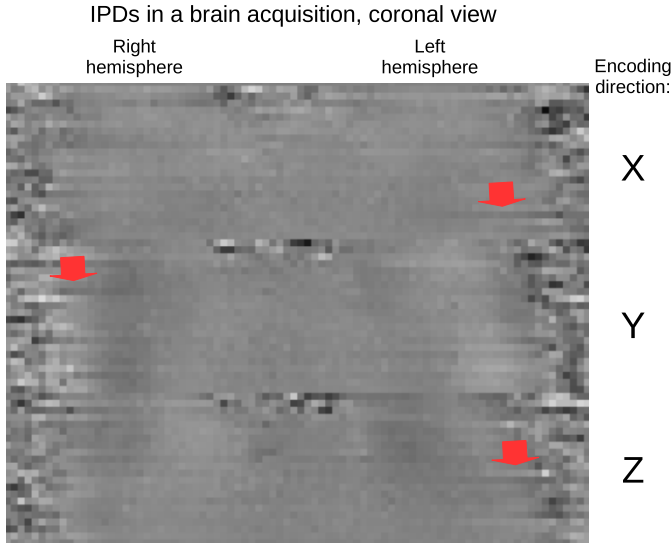


Fig. 1. Example interslice phase discontinuities (IPDs) from an MRE clinical brain acquisition in coronal view. The data is corrupted by a “streaking” artifact proceeding from left to right in this view. Some particularly strong streaks are highlighted with red arrows.

MRI imaging, is well established (e.g. Greitz *et al.* [9], Soellinger *et al.* [36], Hirsch *et al.* [12]). MRE acquisitions acquire a volumetric time series (i.e. 4D acquisition) of phase images and usually do so slice-wise; acquisition of the needed slices occurs over multiple cardiac cycles; consequently neighboring slices are susceptible to shifting of phase, relative to each other, due to cardiovascular displacements. We here consider two kinds of artifacts from this pulsatile motion:

- 1) *Displacement*. Overall displacement of the brain due to cardiac pulsations shifts the encoded wave at each slice.
- 2) *Regional variation in displacement*. The scope of the displacement will further be scaled by anatomical compliance, and therefore in addition to global shifts in the waveform by slice, some regional variation will be present.

An example of IPDs as they appear in a clinical brain acquisition is shown in Figure 1. They appear as “streaks” across the slice, although the severity of the discontinuity is constantly changing as the phases of the neighboring slices alter their distances.

Interslice phase discontinuities have received scant attention in the previous literature. As an early solution the problem was circumvented by analyzing data in-plane, substituting in-plane derivatives for the full 3D range of derivatives (e.g. Manduca *et al.* [19], Papazoglou *et al.* [28]). Such an approach may still be warranted in situations where simplicity is desired, e.g. rapid or real-time processing. However, such an approach will likely underestimate the spatial derivatives of the wavefield, as true wave propagation is in 3D. This will cause a general overestimation of wavenumber. Further it is a source of variance as the wave may be propagating at any angle relative to the plane.

More recently, various efforts to handle IPDs in 3D have emerged. Murphy *et al.* [23] reported artifact reduction by high-passing the 2D slices of complex wave data; Dittmann *et al.* [5] applied a cosine-domain smoothing filter

along the  $z$  axis prior to in-plane low-pass filtering. What both high-pass and low-pass methods have in common is that, by filtering along some axes differently than others, sensor noise becomes anisotropic and correlated. This confounds blind noise estimators and prevents the application of many of the key findings of optimality in denoising (e.g. Donoho *et al.* [6]). Because MRE post-processing incorporates a matrix inversion, it is highly sensitive to choice of denoising parameters, and the inability to optimize denoising is a significant drawback.

Barnhill *et al.* [2] used dualtree-wavelet-domain denoising on the  $z$  axis followed by denoising in the  $xy$  plane, calibrated by Principal Component Analysis (PCA)-based blind noise estimation. As complex dualtree wavelets have been shown to be “optimal” for complex waves with discontinuities [34] this approach is a less lossy solution than smoothing, in a more suitable domain, and the first MRE denoising approach which uses adaptive noise estimation. However, as  $z$  and  $xy$  are denoised separately, the method still requires empirical calibration between the two stages of the process.

What is needed to enable an optimal MRE denoising in full 3D is a method that removes interslice discontinuities while near-losslessly preserving true displacements and the original, uncorrupted sensor noise. In the present study such a procedure was developed, summarized as follows, to approach this goal.

**Dejitter:** We model for the first time the IPD problem as a *dejitter* problem. We define jitter as the displacement of the in-plane data  $d_{xy}$  at  $z$  coordinate  $z_{k+1}$  as compared to  $d_{xy}$  at  $z$  coordinate  $z_k$ , without significant shape change between  $z_k$  and  $z_{k+1}$ . A dejittering algorithm is aimed at reconstructing the relative displacements in an image or volume, restoring the image to coherence. In the present circumstances, the complex wave data  $\mathbf{U}_{x,y,z}$  are not physically displaced, rather the phase  $\arg(\mathbf{U}_{x,y,z_{k+1}})$  is displaced relative to  $\arg(\mathbf{U}_{x,y,z_k})$ . The true phase relationship can therefore be restored by restoring the phase of the image to coherence, which we call dejittering the complex wave field on the sphere. To do this we devise a novel dejitter methodology, generalizing the dejitter methodology found in Nikolova [26], and apply it to the phase space of 3D complex-valued volumes.

**Filter:** Phase shifts from cardiac motion will not impact the slice uniformly, but will scale with mechanical and physiological properties of the tissue. While this shift will mostly be continuous slice to slice, because the tissue properties are mostly continuous, it can create slight additional differences between neighboring slices that the inversion problem is sensitive to. This artifact is handled by transforming the data into the wavelet domain, where the artifact will be isolated in a particular frequency range of a particular bin of coefficients as described below.

Both methodologies are one-iteration techniques and consequently well-suited for clinical applications.

The two steps are first validated by application to a ground-truth Finite Element Method (FEM)-based brain phantom. The phantom is used to calibrate two parameters in the pipeline, the dejitter norm  $\alpha$  and the wavelet highpass threshold  $\omega_c$ , by minimizing root mean square error (RMSE) against

the ground truth. The two methods are then compared with two techniques from the literature on a cohort of 48 healthy brain acquisitions; images and summary statistics by cohort by method are compared.

Our major contributions are: (1) modeling of the IPD problem as a dejitter problem; (2) development of a novel, efficient and objective way to solve IPDs; (3) implementation of the new method in a simple 2 step noniterative algorithm; (4) validation of the method on a ground-truth MRE brain phantom; and (5) demonstration of improved performance of the new method, in terms of reduction in statistical dispersion, on a 48-subject cohort.

## II. METHODS

### A. Theory

1) **Magnetic Resonance Elastography:** In MRE an external driver is used to propagate harmonic motion through the region of interest (ROI) of the MRE acquisition. An isochromat  $u$  at position  $(x, y, z)$  in the image thus undergoes harmonic motion with wavenumber  $k$  and phase offset  $\Phi_0$  about an equilibrium position  $\mathbf{u}(x, y, z, t_0)$

$$\mathbf{u}(x, y, z, t) = \mathbf{u}(x, y, z, t_0) + A \cos(kt + \Phi_0) \quad (1)$$

and one of several shapes of “motion-encoding gradients” is programmed to switch in synchrony with the driving frequency  $\omega = 2\pi/k$  (examples include boxcars, trapezoids, or sinusoids [13]). In the presence of a gradient field  $\mathbf{G}(t)$ , an isochromat with vector trajectory  $\mathbf{u}(t)$  will accumulate phase  $\Phi(t)$

$$\Phi(t) = \Phi(t_0) + \gamma \int_{t_0}^t \mathbf{G}(t') \cdot \mathbf{u}(t') dt' \quad (2)$$

where  $\gamma$  is the gyromagnetic ratio of the specific nuclei. This encodes the instantaneous shear displacements into the magnetic resonance imaging (MRI) phase image. Acquisitions are acquired at  $T$  evenly spaced time steps, in each of three encoding directions  $x, y, z$ , delivering a 4D *ciné* of the shear wave motion similar to those acquired in cardiac MRI [30]. As the data are known to be time-harmonic, this 4D, real-valued *ciné* can be reduced to a 3D, complex-valued time-harmonic field containing the displacements at the experimental driving frequency  $\omega_{exp}$ . First a voxel-wise, temporal discrete Fourier transform (DFT)

$$U(x, y, z, \omega) = \sum_{t=0}^{T-1} \exp(i\omega_0 t - i\omega t) \cdot u(x, y, z, t) \quad (3)$$

is applied, where  $i = \sqrt{-1}$ ,  $u$  is the 4D volumetric scalar *ciné* of one Cartesian displacement component of  $\mathbf{u}$  from Equation 1, and  $U$  is the temporal-axis Fourier transform of  $u$ . Then, only the component of  $U$  corresponding to the experimental driving frequency  $\omega_{exp}$ , that is, the 3D complex scalar field  $U(x, y, z, \omega_{exp})$ , is retained. This procedure can be repeated to acquire displacements in the  $x, y$  and  $z$  directions of polarization which, when combined, yields a vector-valued displacement field  $\mathbf{U}$ .  $\mathbf{U}$  can then be inverted to obtain local

estimates of intrinsic tissue viscoelasticity using the time-harmonic displacement form of the Navier-Lamé equation for isotropic solids:

$$(\mu(U_{k,l} + U_{l,k}))_{,l} + (\lambda \operatorname{div} \mathbf{U})_{,k} = -\rho\omega^2 \mathbf{U} \quad (4)$$

where  $\mu$  and  $\lambda$  are the two Lamé parameters,  $\rho$  is density,  $\operatorname{div}$  is the divergence operator, and  $k$  and  $l$  index the three spatial dimensions. Here in Equation 4, the exposure of the results to interslice discontinuities can be seen, as  $k$  and  $l$  index all three axes. Consequently, discontinuities between the slices of the time-harmonic volume acquisition will cause mis-estimation of the derivatives containing a  $z$  component. To see straightforwardly how this will impact MRE stiffness estimates, consider the reformulation of this equation with the divergence of the field removed, and the gradient of  $\mu$  neglected,

$$\mu = -\frac{\rho\omega^2 \mathbf{U}}{\nabla^2 \mathbf{U}} \quad (5)$$

a common simplification known as Algebraic Helmholtz Inversion (AHI). Here the impact of the mis-estimation of the  $z$  gradients on the estimate of  $\mu$  becomes clear: as the derivative estimate  $\nabla^2 \mathbf{U}$  is artificially inflated due to interslice noise, the stiffness estimate  $\mu$  will artificially drop.

2) **Modeling IPDs:** Per [10], the noise of the above MRI phase field,  $u(x, y, z, t)$ , can be approximated as Gaussian for SNR (defined here as the power of the signal over the power of the noise) higher than 2 dB. By propagation of uncertainties (or by the spherical symmetry of the multivariate Gaussian), the noise distribution of the complex wave field  $\mathbf{U}(x, y, z, \omega)$  will also be Gaussian. As the DFT in Equation 3 filters the data to leave only the periodic motion behavior,  $\mathbf{U}(x, y, z, \omega)$  can be described with a plane wave model [29]

$$U_i = U_{0i} \exp(i\mathbf{k} \cdot \mathbf{x}) \quad (6)$$

where vector components  $U_i$  are scaled and offset with constants  $U_{0i}$  and  $k$  is the vector wavenumber. To incorporate the interslice phase discontinuity (IPD) the field undergoes a linear transformation wherein the phase of the wave is shifted by some factor  $\psi$  such that

$$U_i = U_{0i} \exp(i\mathbf{k} \cdot \mathbf{x} + \psi) \quad (7)$$

and  $\psi$  can be decomposed into a product of the form  $\psi = kc$  containing piecewise-constant term  $k$  and a slow-varying compliance coefficient  $c$ . Each is discussed below.

**Constant global shift**  $k$  is a shift of the field that is constant along  $xy$  and random between  $[0, 2\pi)$  along  $z$ , representing artifact (1) in the Introduction, capturing global change in the phase of the slice due to acquiring the slices at varying points in the cardiac cycle. This effect is removed with the “Phase-Based DeJitter” technique described below.

**Slow-varying deformation**  $c$  is an additional slow-varying deformation field, representing artifact (2) in the Introduction, to capture the physiological dependence of this shift on the compliance of the tissue. This is removed with the “Wavelet-Based Physiological Noise Removal” technique described below.  $c$  is based on physiology

and is therefore not random along  $z$  but continuous volumetrically, so after dejitter, this error would be expected to be minor, but may still impact the wave inversion.

**3) Phase-Based Dejitter:** For the dejitter step, following our definition presented in Section I, lines along the  $z$  axis of the complex wave field are modeled as pieces of 1D, 2nd order smooth polynomials within a globally non-smooth function, that have been jittered by arbitrary global phase shifts applied to each  $xy$  slice. The slices are then aligned by minimizing  $z$  axis second differences over an appropriate function. A related approach was developed by Nikolova [26]. Here, we generalize this approach to the phase of 3D complex-valued images by evaluating:

$$\begin{aligned} \hat{d}_i &= \operatorname{argmin}\{\mathcal{I}(d_i) : d_i \in \{0, \dots, 2\pi\}\} \\ \mathcal{I}(d_i) &= \sum_{j=0}^{M \times N} \left| \operatorname{arg}\left\{ \frac{g_i(j - d_i) \hat{f}_{i-2}(j)}{2 \hat{f}_{i-1}(j)} \right\} \right|^\alpha \end{aligned} \quad (8)$$

In this model,  $g$  is the line to be dejittered and  $\hat{f}_{i-1}$  and  $\hat{f}_{i-2}$  are previously dejittered slices of the image, each containing  $M \times N$  pixels, and  $\alpha$  is the parameter commonly called the norm. The multiplications of  $g_i$  and  $\hat{f}_{i-2}$  mean that their phases are added in the phase plane, and the division by  $2 \hat{f}_{i-1}$  subtracts double the phase of  $\hat{f}_{i-1}$ , hence the summed term is a phase-plane equivalent of the  $\alpha$ -norm of the common finite difference approximation to the second derivative whose stencil takes the form  $[1 \ -2 \ 1]$ . The argument of this complex quantity, as it measures phase angle, is then evaluated. This derivative is calculated for each available pixel  $d_i$  in  $g$ . The range of  $d_i$  is divided into a discrete number of bins (here 256), enabling minimization by exhaustive search.

As second-order estimation is not possible to dejitter the second slice to the first, the initial step of dejittering the second slice is done with a first-order difference. The method is illustrated on a heavily jittered *in vivo* brain in Figure 2.

**4) Wavelet-Based Physiological Noise Removal:** For the second step discontinuities from physiological noise are removed. As mentioned before, such artifact is not uniform across the slice but varies proportional to tissue compliance and functional physiology, as these will alter wavelength. To address any additional artifact between slices, two properties of the artifact can be exploited:

- It is slowly varying across the  $xy$  plane
- It is discontinuous on the  $z$  axis

Bearing this in mind we consider the decomposition of  $U_i$  with a multi-resolution analysis (MRA) [18], where in 1D

$$M_{1D} = \sum_{k \in \mathbb{Z}} c_k \phi_k + \sum_{k \in \mathbb{Z}} d_k \psi_k \quad (9)$$

where  $M$  is the MRA,  $\phi$  is a low-pass scaling function and  $\psi$  is a high-pass wavelet function at logarithmic scale  $k$ . Taking a linear filtering perspective, this expands in 3D to

$$M_{xyz} = \{U_i \star \phi_{kx} \star \phi_{ky} \star \phi_{kz}, U_i \star \phi_{kx} \star \phi_{ky} \star \psi_{kz}, \dots, U_i \star \psi_{kx} \star \psi_{ky} \star \psi_{kz}\} \quad (10)$$

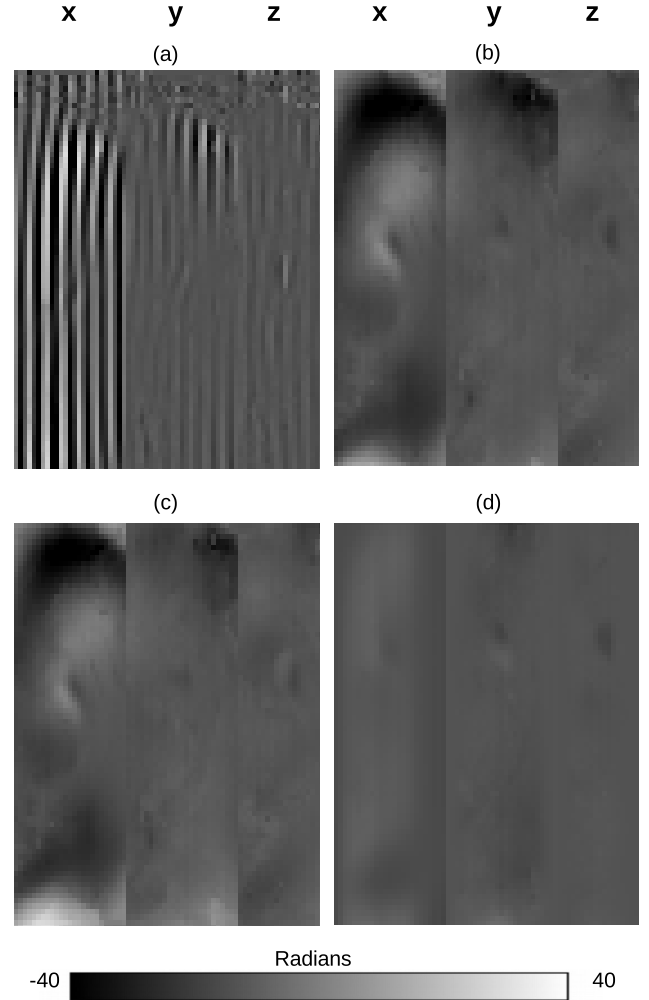


**Fig. 2.** Illustration of the dejitter algorithm on an MRE acquisition of a human brain: (a) heavily jittered MRE acquisition; (b) ground-truth dejittering; (c) dejitter with current method; (d) error from ground truth.

where the  $\star$  operator denotes a periodic convolution. That is, the MRA at level  $k$  consists of eight combinatoric convolutions with low-pass  $\phi$  and high-pass  $\psi$ . An artifact which varies slowly on  $xy$  but quickly on  $z$  will be captured in the  $\phi\phi\psi$  coefficients, in which  $xy$  is lowpass-filtered but  $z$  is highpass-filtered, and not present in the other images. The slowly-varying in-plane gradients in  $\phi\phi\psi$  are preferably removed without removal of the high-frequency coefficients in  $\phi\phi\psi$ , which will be both the sensor noise and high-frequency edges that are desired for further post-processing. Therefore rather than a usual wavelet thresholding technique, we remove any remaining IPDs and preserve the sharp edges by applying an in-plane high-pass filter to  $\phi\phi\psi$  prior to the inverse MRA. Daubechies 3 wavelets were used for the decomposition as shown in Figure 3. The settings for the highpass filter are calibrated below in the Experiment.

The wavelet step of the IPD removal is illustrated on the FEM brain model in Figure 4. Here a slow-moving wave image contains warping in a central slice, creating an IPD. The figure shows that this IPD is not present in the scaling image, or 7 of the 8 bins of the discrete wavelet transform (DWT), but is picked up only by the  $\phi\phi\psi$  bin. When the  $\phi\phi\psi$  is high-passed,



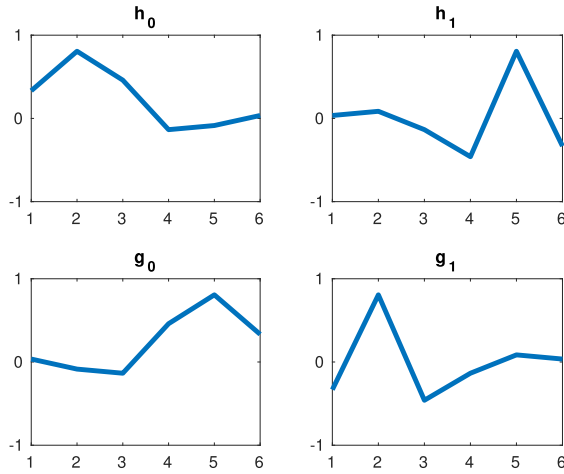


Fig. 3. The Daubechies-3 filters used in the physiological noise removal method.

the IPD is removed. The magnitude of the signal in  $\phi\phi\psi$  is now comparable to the other bins.

Real decimated wavelets are often considered suboptimal for 3D images as they preferentially identify features along the axes [33], and for typical denoising some other bases show better properties (e.g. Kutyniok *et al.* [17]). For IPDs, however, the properties of this simpler transform are helpful, with the  $\phi\phi\psi$  image ideally suited to capture slow-varying interslice-related artifact with minimal loss.

## B. Evaluation

To evaluate the IPD removal techniques in a controlled fashion, they are first applied to an FEM brain model. The model is used for calibration of the two free variables in each step ( $\alpha$  in the case of the dejitter, and  $\omega_c$  in the case of the wavelet discontinuity removal.) To evaluate the benefits of the method *in vivo*, four different IPD removal strategies are then tried on a cohort of 48 brain MRE acquisitions and compared.

## C. FEM Brain Model

A 3D model of human brain was developed from segmented images of a healthy human, consisting of scalp, skull, cerebrospinal fluid, gray matter and white matter [1]. Furthermore, since *falx cerebri* affects wave displacement fields severely, segmentation of *falx cerebri* was added manually. The model was imported to COMSOL Multiphysics (COMSOL, Stockholm, Sweden) finite element method (FEM) software and Young's modulus, Poisson's ratio and density parameters were assigned to the segmented parts, reported in previous studies [16], [21], [32]. Damping parameters were assigned to gray matter and white matter, using stiffness damping  $\beta$  of Rayleigh damping, similar to a previous study [11]. Stiffness damping was computed using  $\beta = (G''/G')/\omega$ , where  $G'$  is the storage modulus,  $G''$  is the loss modulus and  $\omega$  is the excitation frequency. Frequency domain analysis was performed by rotationally vibrating the head around y-axis (anterior-posterior), similar to head bobble motion or the

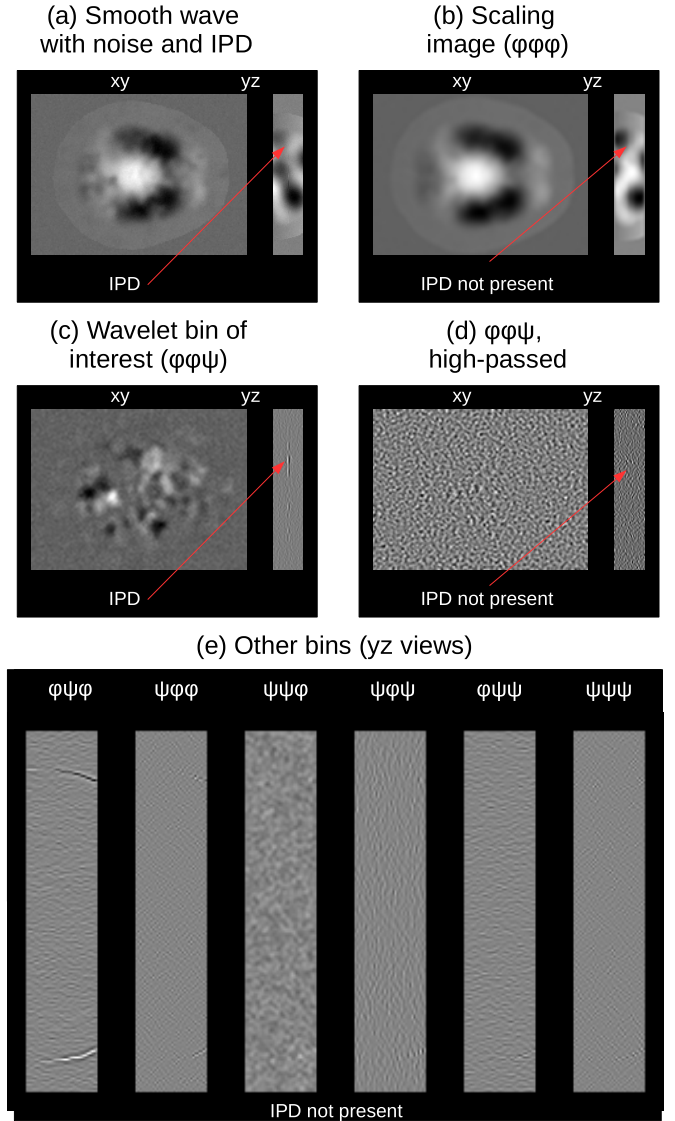


Fig. 4. Illustration of the physiological noise removal technique. (a) Smoothly oscillating image with a discontinuity. (b) Scaling image of the DWT does not contain the discontinuity. (c)  $\phi\phi\psi$  contains the discontinuity. (d) Highpassing removes the discontinuity. (e) No other bin contains the discontinuity.

excitation of a bite actuator. The excitation frequency was swept from 24 to 60  $Hz$  with 4  $Hz$  increments. Applied peak input displacement was  $10\mu m$ . Mesh sizes were chosen to satisfy having at least 10 mesh elements per wavelength. Complex displacement field data were exported with  $1.5mm$  isotropic voxels. A central slice of the model is shown in Figure 5.

## D. Calibration of $\alpha$

Nikolova [26] used Monte Carlo analysis to find an optimal  $\alpha$  of 0.5 for dejittering of real video. However, an optimal  $\alpha$  will depend on image properties as well as amount of similarity between neighboring lines. Here we re-evaluate  $\alpha$  in the context of our 3D, phase-based dejitter with a calibration step. We evaluated 1000 trials of each image at each  $\alpha$ , jittering the slices by offsetting the phase of the complex wave of each

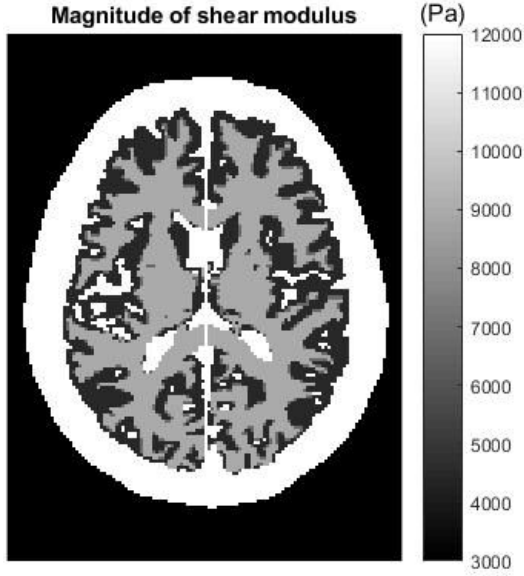


Fig. 5. Central slice of the FEM brain model.

slice with a random value  $c$ ,  $0 < c < 2\pi$ . Pseudo-code for this calibration is as follows:

- for  $\alpha = 0.05:0.01:2$ 
  - for trial = 1:1000
    - \* for image = 1:30
      - 1) Randomly jitter slices 2:end
      - 2) Dejitter with  $\alpha$
      - 3) Measure RMSE against ground truth
    - Evaluate global RMSE for  $\alpha$
- Choose  $\alpha$  with lowest RMSE

#### E. Calibration of $\omega_c$

A high-pass cutoff spatial frequency  $\omega_c$  was calibrated for the highpass-filtering of  $\phi\phi\psi$  wavelet coefficients described above. We evaluate a normalized  $\omega_c$  coefficient for the high-pass filter from 0.01 to 0.25 in increments of 0.01, where 0 removes no information and 1 removes all frequencies. Each component of each driving frequency of the model was subjected to a random warping process. Pseudo-code for this calibration is as follows:

- for  $\omega_c = 0.01:0.01:0.25$ 
  - for image = 1:30
    - \* Create random noise image,  $\sigma = 2\pi$
    - \* Smooth with 2D Gaussian spatial filter,  $\sigma = 3px$
    - \* Multiply phase of central slice by smoothed noise field
    - \* Remove discontinuity using the technique described in Section II-A.4
    - \* Calculate RMSE
- Calculate  $\omega_c$  with minimum RMSE for each image
- Choose cutoff with lowest median RMSE

#### F. Elastogram Evaluation

Finally we studied the impact of the IPD removal strategy on stiffness estimation. We compared four interslice strategies

against the FEM brain model described in Section II-C with increasing levels of jitter. The four strategies were also compared on an *in vivo* brain cohort of 48 subjects.

1) *Comparative Slice Removal Strategies*: It was expected that the present IPD removal method would improve both range and stability of elastogram results against the neglect of IPDs. It was however imperative to evaluate against other schemes developed to handle IPDs. Here we compare the present technique against three contrasting techniques:

- an anisotropic wavelet-based method, in which the  $z$  axis is denoised prior to the  $xy$  plane, developed in Barnhill *et al.* [2], called here the Anisotropic method;
- The “control condition” with no IPD removal, called here Neglect;
- and a purely in-plane pipeline developed in Fehlner *et al.* [7], which avoids the issue of IPDs by only processing images in-plane, but neglects the wave derivatives in the  $z$  direction, called here 2D;

2) *Simulations With Increasing Jitter*: The FEM model described in Section II-C was given artificial jitter by shifting the wave phase of each slice by a random amount with a prescribed standard deviation  $\sigma$ .  $\sigma$  was varied from 0% to 20% of the  $2\pi$  phase circle in increments of 2%. Each “shuffled” simulation was subjected to IPD removal with the proposed method as well as the comparison schemes. Elastograms were then produced using the Helmholtz inversion method described in [3].

MRE inversion schemes do not recover detail on the fineness of scale of the brain phantom. Consequently we compared values within a homogeneous region of white matter selected from the original model without reference to the recovery, as such a region was expected to avoid partial-volume effects.

3) *In Vivo Cohort*: We additionally applied the four contrasting methods to a cohort of 48 subjects (ages 18-60, 26 women) whose acquisition details were described in Fehlner *et al.* [7]; subjects were vibrated at 30, 40, and 50Hz using an acquisition sequence consisting of 15 slices of 2mm isotropic voxels of brain acquired axially. Elastograms were obtained with the same method. We evaluate the performance of the various methods by looking at mean and dispersion statistics across the cohort for each method. Based on previous literature (e.g. Dittmann *et al.* [5]) we expected median elasticity estimates at approximately 40Hz to be in the range of 1.6 to 1.8 kPa.

### III. RESULTS

#### A. Calibration of $\alpha$

Figure 6 shows results by trial and  $\alpha$ -value for calculation of the dejittering parameter  $\alpha$ . Across multiple trials with random jitter, the RMSE varies, for example at  $\alpha = 0.3$  the RMSE ranges from .0014 to .1064 radians, with mean of 0.0218 radians. The data further show a critical point between  $\alpha = 1.3$  and  $\alpha = 1.4$  wherein the error rises considerably. Minimum error was found at  $\alpha = 1.0$ , with a mean RMSE of 0.0167 radians, and this value was used for the cohort experiment. However the overall finding is that norms

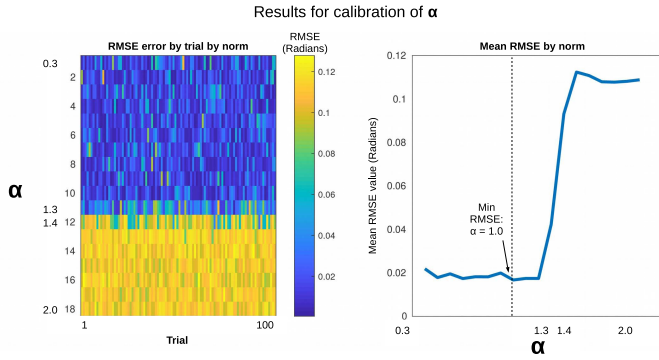


Fig. 6. Results for calibration of  $\alpha$ .  $\alpha$  results are comparable until a “critical point” of 1.3, at which point the RMSE rises; optimal  $\alpha$  was 1.0.

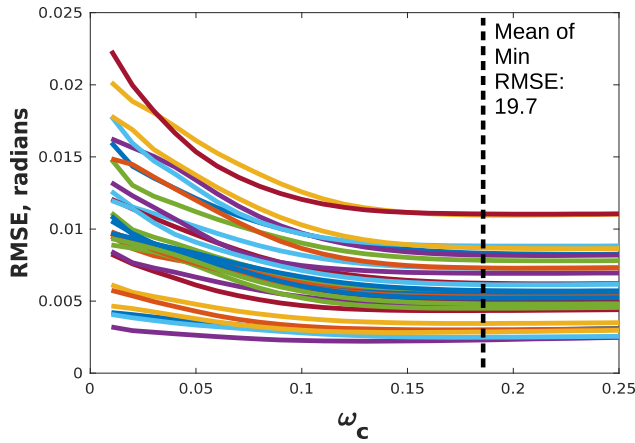


Fig. 7. Results for calibration of  $\omega_c$ . For all 30 model images, mean optimal RMSE cutoff was 0.197.

below  $\alpha = 1.4$  are effectively interchangeable, and all perform significantly better than the popular 2-norm.

### B. Calibration of $\omega_c$

Results for the calibration of the normalized highpass cutoff  $\omega_c$  are shown in Figure 7. Each colored line represents one of the 30 wave images in the FEM model. As the cutoff is increased from  $\omega_c = 0.01$ , the error caused by the warping slice decreases; the result has reached a clear equilibrium by a cutoff of  $\omega_c = 0.2$ . The cutoff value which minimized RMSE by image ranged from 13 to 23; the mean of these cut-offs was 0.197, with mean RMSE of .002 radians. Consequently, 0.197 was applied in the *in vivo* experiment.

### C. Inversion of FEM Model With Progressive Jitter

Overall results for the progressive jitter inversion recoveries are shown in Figure 8. Prescribed values are shown in green. IPD removal convincingly reproduced the prescribed value at all levels of jitter severity with a standard deviation from prescribed of 1.7%. The previous Anisotropic strategy is equally effective until around 4% jitter, then drops in value. Neglect produces values too low at all levels of jitter, decreasing with the amount of jitter. The 2D recovery was immune to amount

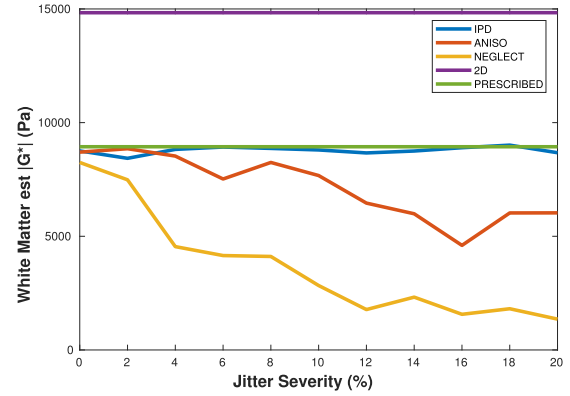


Fig. 8. Estimated elasticity within a homogeneous region of white matter, as prescribed by the FEM model (green) and as recovered by each of four IPD handling strategies.

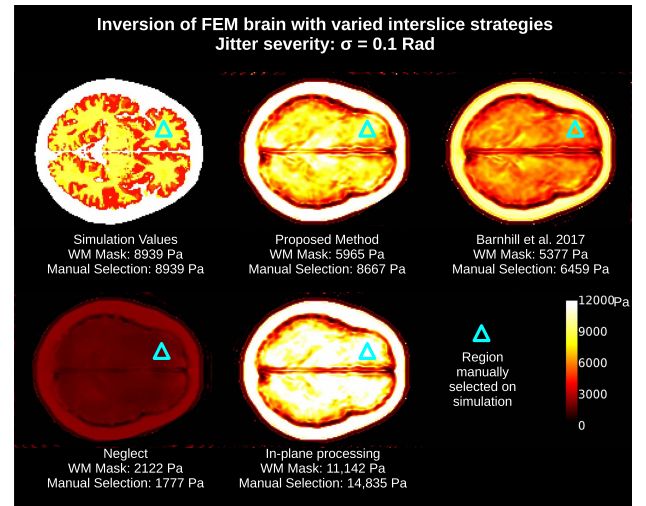


Fig. 9. Estimated elasticity within a homogeneous region of white matter, as prescribed by the FEM model (green) and as recovered by each of four IPD handling strategies.

of jitter as expected, but produced a 66% overestimation of the values.

These results are illustrated for a single slice of each result, at 10% jitter, in Figure 9. It can be seen that our widely used recovery method only gives a rough approximation of the fine detail within the FEM model. However, with the IPD method a small region, manually selected prior to inversion, of homogeneous tissue is within 3% of model values. For a point of comparison, we also report results when the white matter region of the model is used as a mask, and this value is beneath the prescribed value due to partial-volume effects.

### D. Evaluation of In Vivo Cohort

Table I shows summary statistics for the cohort comparisons. IPD Removal and Anisotropic methods show median values consistent with each other and with expectations: the 2D median is 6.25% higher than the IPD removal method while the Anisotropic median is 4.86% higher. Neglect as expected is substantially (16.8%) lower due to disruption of the wavelengths on the  $z$  axis. Figure 10 shows the distribution of values with error bars at the .05 and .95 percentiles.

TABLE I  
SUMMARY STATISTICS FOR THE COHORT COMPARISON

	$ G^* $			
	Median	5th Pct.	95th Pct.	Range
IPD Removal	1873 Pa	1573 Pa	2142 Pa	42.1 %
Neglect	1559	1314	1821	49.8%
2D	1990	1587	2411	56.4 %
Anisotropic	1964	1630	2325	57.7 %

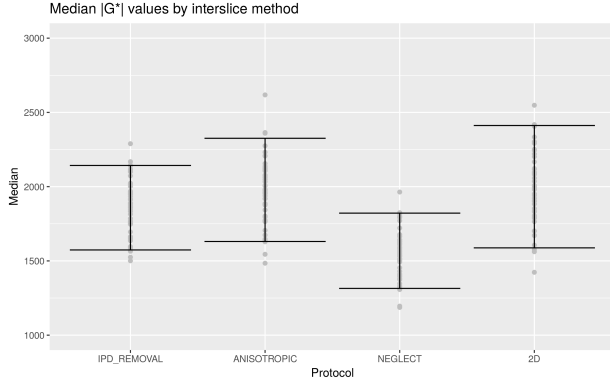


Fig. 10. Value distributions for the cohort comparison: proposed technique, anisotropic IPD removal, neglect of IPDS, and 2D processing respectively.

While the new IPD removal method produces similar medians to the two established methods (2D and Anisotropic), there is a striking difference in the dispersion. In particular, the range of the results for IPD removal method (788 Pa) is 29% less than the Anisotropic method and 31% less than the 2D method. The results are illustrated for an example slice in Figure 11. As with the cohort, the relative underestimation of  $|G^*|$  by neglect is visible; here also, the shear stiffness is slightly higher for Anisotropic and 2D than for IPD removal.

#### IV. DISCUSSION

The present method applies a two-step process to de-jitter MRE phase acquisitions. First the slices are de-jittered by modeling lines on the  $z$  axis of the complex image as having piecewise-smooth phase, then aligning each ensuing slice by applying the phase shift that minimizes a norm-like parameter  $\alpha$ . Our calibration of  $\alpha$  confirmed the finding of Nikolova [26] that a non-convex norm outperforms the  $l2$  norm. We further found an interesting “critical point” at  $\alpha = 1.3$ , a value above which the error profile qualitatively shifts. Our overall finding is that a convex norm  $\leq 1.3$  will suffice for de-jitter in MRE.

Next the slices have remaining discontinuities removed by applying in-plane high pass filters on a selected bin of the real DWT of the field. Here it was found that normalized frequency cutoffs in the range of 0.15 – 0.20 suffice to remove the discontinuity and minimize error relative to ground truth.

The use of the FEM model for inversion recovery with progressive levels of jitter produced several insights of potential

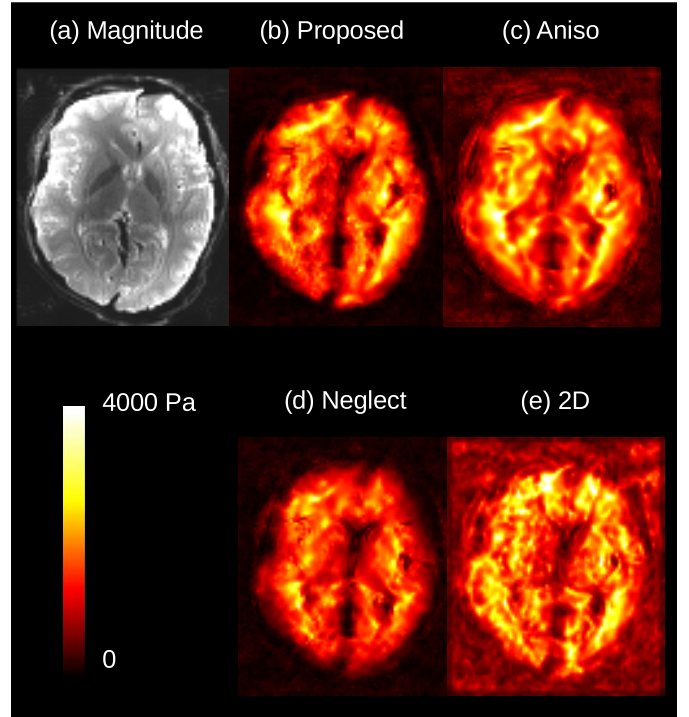


Fig. 11.  $|G^*|$  maps for the central slice of a representative subject brain acquisition. The (a) T2\* weighted magnitude image is for the same slice as the four interslice processing methods: (b) proposed de-jitter method, (c) Anisotropic IPD removal, (d) neglect of IPDs, (e) 2D processing.

interest to the community. As regards the present investigation, the ability of the proposed IPD strategy to recover true values against strong jitter is clearly shown. It is also clear that neglect of IPDs fails and the method of [2] only handles relatively small amounts of jitter. It is expected that an in-plane evaluation will underestimate the derivatives of the 3D wave motion, and produce an overshoot in elasticity estimate. The overshoot from this model is much higher than that found *in vivo*. This suggests that wave actuation *in vivo* is, in general, sufficiently planar that the mis-estimate from in-plane wavenumber estimation is tempered, and in principle it could be effectively eliminated [4]. However this model is a good reminder that without the use of 3D derivatives, MRE values are at risk of severe mis-estimation and caution is required.

We are pleased to present the first published results from this FEM brain model which may prove of broader use to the community. The model reproduces well the fine detail of estimated brain tissue stiffness. Reconstructions from this model, even with state of the art methods, highlight the current limitations of the field in terms of effective resolution in stiffness estimation, and give a good sense for the community of what can be expected with brain MRE. In particular, exact recovery only occurs in homogeneous regions that avoid partial volume effects, a finding which supports the practice of erosion prior to measurement found in Murphy *et al.* [24] and in accordance with clinical MRE protocols which suggest the use of manually selected regions [20]. This model brain may make a good benchmark against which claims of fine feature recovery in the brain can be measured. In particular,



recent papers claiming robust measurements of small brain features (e.g. [15]) may wish to validate their claims by showing that fine details in this or a similar brain model can be visibly recovered. The brain model can be obtained at the Charité web apps site <https://bioqic-apps.charite.de/downloads>.

Finally an *in vivo* cohort of 48 subjects was investigated to evaluate the effectiveness of the IPD removal as compared to other best practices in a clinical context. Median results for IPD removal were comparable to two other established methods, an anisotropic noise removal method and an in-plane or 2D inversion method. However, IPD removal considerably reduced the dispersion of the results as compared to the other methods. For neglect, the unpredictability of the jitter is an additional source of variance, and median results are too low as expected. In the case of the 2D method, the 2D methods cannot estimate wavelength in the  $z$  direction as discussed above. The anisotropic method shows better stability than the 2D, but the separate calibration of  $z$  and  $xy$  appears inherently less stable than a fully 3D denoising method such as that enabled by IPD removal, and likely shows slightly higher stiffness results *in vivo* due to smoothing in  $z$ . All these findings are tempered by the fact that brain MRE is widely reported to contain considerable natural variation (e.g. Barnhill *et al.* [3] and Hiscox *et al.* [14]). However, these differences when controlling for all other factors complement the findings of the more controlled experiments with an FEM model above.

The proposed IPD removal method has some limitations. The dejitter is in principle lossless, but against numerous trials with random jitter, showed some range of error. The physiological noise removal cannot replace the lost information within slices where a slice-wise artifact has been stripped out, which also leaves some error against an IPD-free model. Further, in the case of a large amount of physiological warping, the dejitter would not be perfectly fitted. However, compliance-related artifact will be mostly consistent slice to slice and we would expect this variation to be relatively small. Despite these limitations, the method outperforms two other state-of-the-art attempts to handle such IPD artifacts.

The present study focused on brain, partly because brain MRE has established 3D analysis as a “common principle” [25], while commercial and experimental abdominal sequences often focus on 2D wave inversion for reasons of both historical validation and clinical convenience. Nonetheless the present methods are equally applicable to other MRE acquisitions where physiological activity may cause slight alterations to the phase during slice-wise acquisitions.

In summary, the present IPD removal technique is likely a valuable step in future MRE image processing pipelines, enables improved approaches to denoising in future MRE studies, and its non-iterative nature ensures it can be applied even within clinical exams on short time frames.

#### ACKNOWLEDGMENT

The authors were honored to have co-authored this publication with the great mathematician Mila Nikolova and dedicate it to her memory.

#### REFERENCES

- [1] B. Aubert-Broche, A. C. Evans, and L. Collins, “A new improved version of the realistic digital brain phantom,” *NeuroImage*, vol. 32, no. 1, pp. 138–145, 2006.
- [2] E. Barnhill *et al.*, “Nonlinear multiscale regularisation in MR elastography: Towards fine feature mapping,” *Med. Image Anal.*, vol. 35, pp. 133–145, Jan. 2017.
- [3] E. Barnhill, P. J. Davies, C. Ariyurek, A. Fehlnner, J. Braun, and I. Sack, “Heterogeneous multifrequency direct inversion (HMDI) for magnetic resonance elastography with application to a clinical brain exam,” *Med. Image Anal.*, vol. 46, pp. 180–188, May 2018.
- [4] J. Bishop, A. Samani, J. Sciarretta, and D. B. Plewes, “Two-dimensional MR elastography with linear inversion reconstruction: Methodology and noise analysis,” *Phys. Med. Biol.*, vol. 45, no. 8, p. 2081, 2000.
- [5] F. Dittmann, S. Hirsch, H. Tzschätzsch, J. Guo, J. Braun, and I. Sack, “*In vivo* wideband multifrequency MR elastography of the human brain and liver,” *Magn. Reson. Med.*, vol. 76, no. 4, pp. 1116–1126, 2016.
- [6] D. L. Donoho, I. M. Johnstone, G. Kerkycharian, and D. Picard, “Wavelet shrinkage: Asymptopia?” *J. Roy. Stat. Soc. B, Methodol.*, vol. 57, no. 2, pp. 301–369, 1995.
- [7] A. Fehlnner *et al.*, “Higher-resolution MR elastography reveals early mechanical signatures of neuroinflammation in patients with clinically isolated syndrome,” *J. Magn. Reson. Imag.*, vol. 44, no. 1, pp. 51–58, 2016.
- [8] A. Fehlnner *et al.*, “Increasing the spatial resolution and sensitivity of magnetic resonance elastography by correcting for subject motion and susceptibility-induced image distortions,” *J. Magn. Reson. Imag.*, vol. 46, no. 1, pp. 134–141, 2017.
- [9] D. Greitz, R. Wirestam, A. Franck, B. Nordell, C. Thomsen, and F. Ståhlberg, “Pulsatile brain movement and associated hydrodynamics studied by magnetic resonance phase imaging,” *Neuroradiology*, vol. 34, no. 5, pp. 370–380, 1992.
- [10] H. Gudbjartsson and S. Patz, “The Rician distribution of noisy MRI data,” *Magn. Reson. Med.*, vol. 34, no. 6, pp. 910–914, 1995.
- [11] U. Hamhaber, I. Sack, S. Papazoglou, J. Rump, D. Klatt, and J. Braun, “Three-dimensional analysis of shear wave propagation observed by *in vivo* magnetic resonance elastography of the brain,” *Acta Biomaterialia*, vol. 3, no. 1, pp. 127–137, 2007.
- [12] S. Hirsch, D. Klatt, F. Freimann, M. Scheel, J. Braun, and I. Sack, “*In vivo* measurement of volumetric strain in the human brain induced by arterial pulsation and harmonic waves,” *Magn. Reson. Med.*, vol. 70, no. 3, pp. 671–683, 2013.
- [13] S. Hirsch, J. Braun, and I. Sack, *Magnetic Resonance Elastography: Physical Background and Medical Applications*. Hoboken, NJ, USA: Wiley, 2016.
- [14] L. V. Hiscox *et al.*, “Magnetic resonance elastography (MRE) of the human brain: Technique, findings and clinical applications,” *Phys. Med. Biol.*, vol. 61, no. 24, p. R401, 2016.
- [15] C. L. Johnson *et al.*, “Viscoelasticity of subcortical gray matter structures,” *Hum. Brain Mapping*, vol. 37, no. 12, pp. 4221–4233, 2016.
- [16] S. Kleiven and H. von Holst, “Consequences of head size following trauma to the human head,” *J. Biomech.*, vol. 35, no. 2, pp. 153–160, 2002.
- [17] G. Kutyniok, W.-Q. Lim, and R. Reisenhofer, “Shearlab 3D: Faithful digital shearlet transforms based on compactly supported shearlets,” *ACM Trans. Math. Softw.*, vol. 42, no. 1, p. 5, 2016.
- [18] S. Mallat, *A Wavelet Tour of Signal Processing: The Sparse Way*. New York, NY, USA: Academic, 2008.
- [19] A. Manduca *et al.*, “Magnetic resonance elastography: Non-invasive mapping of tissue elasticity,” *Med. Image Anal.*, vol. 5, pp. 237–254, Dec. 2001.
- [20] Y. K. Mariappan, K. J. Glaser, and R. L. Ehman, “Magnetic resonance elastography: A review,” *Clin. Anatomy*, vol. 23, pp. 497–511, Jul. 2010.
- [21] P. J. McCracken, A. Manduca, J. Felmlee, and R. L. Ehman, “Mechanical transient-based magnetic resonance elastography,” *Magn. Reson. Med.*, vol. 53, no. 3, pp. 628–639, 2005.
- [22] D. W. McRobbie, E. A. Moore, M. J. Graves, and M. R. Prince, *MRI From Picture to Proton*. Cambridge, U.K.: Cambridge Univ. Press, 2007.
- [23] M. C. Murphy, J. Huston, K. J. Glaser, A. Manduca, J. P. Felmlee, and R. L. Ehman, “Phase correction for interslice discontinuities in multislice EPI MR elastography,” in *Proc. 20th ISMRM Annu. Meeting (ISMRM)*, 2012, p. 3426.
- [24] M. C. Murphy *et al.*, “Measuring the characteristic topography of brain stiffness with magnetic resonance elastography,” *PLoS ONE*, vol. 8, no. 12, 2013, Art. no. e81668.

- [25] M. C. Murphy, J. Huston, III, and R. L. Ehman, "MR elastography of the brain and its application in neurological diseases," *NeuroImage*, to be published.
- [26] M. Nikolova, "One-iteration dejittering of digital video images," *J. Vis. Commun. Image Represent.*, vol. 20, no. 4, pp. 254–274, 2009.
- [27] F. Ong *et al.*, "Robust 4D flow denoising using divergence-free wavelet transform," *Magn. Reson. Med.*, vol. 73, no. 2, pp. 828–842, 2015.
- [28] S. Papazoglou, U. Hamhaber, J. Braun, and I. Sack, "Algebraic Helmholtz inversion in planar magnetic resonance elastography," *Phys. Med. Biol.*, vol. 53, no. 12, p. 3147, 2008.
- [29] S. Papazoglou, "Elucidation of isotropic and anisotropic shear elasticity of *in vivo* soft tissue using planar magnetic resonance elastography," Ph.D. dissertation, Dept. Exp. Radiol., Charité Univ. Smedizin Berlin, Berlin, Germany, 2009.
- [30] N. J. Pelc, R. J. Herfkens, A. Shimakawa, and D. R. Enzmann, "Phase contrast cine magnetic resonance imaging," *Magn. Reson. Quart.*, vol. 7, no. 4, pp. 229–254, Oct. 1991.
- [31] K. Riek *et al.*, "Magnetic resonance elastography reveals altered brain viscoelasticity in experimental autoimmune encephalomyelitis," *NeuroImage, Clin.*, vol. 1, no. 1, pp. 81–90, 2012.
- [32] J. S. Ruan, T. Khalil, and A. I. King, "Human head dynamic response to side impact by finite element modeling," *J. Biomech. Eng.*, vol. 113, no. 3, pp. 276–283, 1991.
- [33] I. W. Selesnick and P.-Y. Chen, "Total variation denoising with overlapping group sparsity," in *Proc. IEEE Int. Conf. Acoust., Speech Signal Process. (ICASSP)*, May 2013, pp. 5696–5700.
- [34] I. W. Selesnick, R. G. Baraniuk, and N. C. Kingsbury, "The dual-tree complex wavelet transform," *IEEE Signal Process. Mag.*, vol. 22, no. 6, pp. 123–151, Nov. 2005.
- [35] S. M. Smith *et al.*, "Advances in functional and structural MR image analysis and implementation as FSL," *NeuroImage*, vol. 23, pp. S208–S219, Sep. 2004.
- [36] M. Soellinger, A. K. Rutz, S. Kozerke, and P. Boesiger, "3D cine displacement-encoded MRI of pulsatile brain motion," *Magn. Reson. Med.*, vol. 61, no. 1, pp. 153–162, 2009.
- [37] A. Tobisch, P. F. Neher, M. C. Rowe, K. H. Maier-Hein, and H. Zhang, "Model-based super-resolution of diffusion MRI," in *Computational Diffusion MRI and Brain Connectivity*. Nagoya, Japan: Springer, 2014, pp. 25–34.
- [38] H. Tzschätzsch *et al.*, "Tomoelastography by multifrequency wave number recovery from time-harmonic propagating shear waves," *Med. Image Anal.*, vol. 30, pp. 1–10, May 2016.
- [39] C. S. Zuo, A. Jiang, B. L. Buff, T. G. Mahon, and T. Z. Wong, "Automatic motion correction for breast MR imaging," *Radiology*, vol. 198, no. 3, pp. 903–906, 1996.